

Breaking the linear scaling limit in multi-electron-transfer electrocatalysis through intermediate spillover

Received: 24 September 2023

Accepted: 11 March 2025

Published online: 2 April 2025

 Check for updates

Qilun Wang^{1,16}, Sung-Fu Hung^{2,3,16}, Kejie Lao^{4,5,16}, Xiang Huang⁶, Fuhua Li¹, Hua Bing Tao^{4,5}✉, Hong Bin Yang⁷, Wei Liu⁸, Weijue Wang⁸, Yaqi Cheng⁹, Nozomu Hiraoka¹⁰, Liping Zhang⁶, Junming Zhang⁶, Yuhang Liu⁷, Jiazang Chen¹¹, Yinghua Xu¹², Chenliang Su¹³, Jingguang G. Chen¹⁴✉ & Bin Liu^{1,15}✉

The linear scaling relationships between the adsorption energies of multiple intermediates constrain the maximum reaction activity of heterogeneous catalysis. Here we propose an intermediate spillover strategy to decouple the elementary electron-transfer steps in an electrochemical reaction by building a bi-component interface, thereby independently tuning the corresponding intermediate adsorption at an individual catalytic surface. Taking the electrocatalytic oxygen reduction reaction as an example, oxophilic sites are preferable for activating oxygen molecules, then the adsorbed OH* intermediates spontaneously migrate to the adjacent sites with a weaker oxygen binding energy, where OH* intermediates are further reduced and desorbed to complete the overall catalytic cycle. Consequently, the designed Pd/Ni(OH)₂ catalyst can remarkably elevate the half-wave potential of the oxygen reduction reaction to ~70 mV higher than that of the Pt/C catalyst, surmounting the theoretical overpotential limit of Pd. This design principle highlights an opportunity for utilizing intermediate spillover to break the ubiquitous scaling relationships in multi-step catalytic reactions.

Heterogeneous catalysis currently plays a key role in energy-efficient chemical industries and sustainable technologies, with optimal catalysts readily activating reactants with neither too weak nor too strong binding to intermediates^{1–3}. As a consequence of the progress in applying density functional theory (DFT) to surface chemistry, the adsorption energies of transition states and intermediates have been used to understand bond formation and scission, as well as reactivity trends^{4,5}. Based on bond-order conservation theory, in a complex multi-electron-transfer reaction, the adsorption energies of multiple intermediates on the same active site can be correlated to one another in a linear manner^{6,7}. Although such adsorption-energy scaling relations help in reducing the dimension of a kinetic-model expression

from considering all elementary steps to fewer descriptors and hence accelerate the high-throughput screening of catalysts, they often set a theoretical upper limit on the catalytic activity, which exhibits a volcano-shaped dependence on the adsorption energies of the key intermediates^{8–10}. Moreover, the apices of these volcano relations—the theoretical maxima of catalytic rates—are normally insufficient for practical application requirements^{11–13}. To break the symmetry rules induced by linear scaling relations and climb beyond the tops of the volcanoes, many research efforts have been devoted to tuning the geometric and electronic effects of materials, such as strain engineering, alloying, ligands as well as external forces^{14–18}. However, most current modulation strategies are confined to a typical family of materials and

A full list of affiliations appears at the end of the paper. ✉e-mail: hbtiao@xmu.edu.cn; jgchen@columbia.edu; bliu48@cityu.edu.hk

reactions or only switch the previous relation to another new scaling line, and are often unable to overcome the complexity of structural properties and catalytic routes⁸.

Rather than modifying the single-phase catalytic surface itself, the ideal scenario is to divide a stepwise reaction onto separate catalytic centres with their corresponding optimal adsorption energetics, that is, to locate individual correlated intermediates on independent sites with different functions^{19,20}. As a widespread phenomenon of bi-component catalysts, the spillover of adsorbed species affords a unique opportunity to achieve dynamic intermediate transfer to a secondary site when a critical surface coverage is reached at the primary site²¹. However, successful cases of intermediate spillover in accelerating heterogeneous catalysis remain rare because of the barrier of the free-energy difference between strong adsorption sites and the intermediate deficient components, as well as undesirable interfacial diffusion resistance^{22,23}. Accordingly, an open question remains regarding how to enable this conceptually interesting but practically challenging process under operational conditions. In addition, missing insights into the spillover effect require *in situ* characterization techniques and model catalyst structure design to monitor the dynamic behaviour of catalytic processes at the atomic scale^{24,25}.

In this Article we develop an intermediate-spillover-based tandem reaction pathway to break the activity limit imposed by adsorption-energy scaling relationships in heterogeneous electrocatalysis involving multiple intermediates. This general design principle has been demonstrated on the electrocatalytic oxygen reduction reaction (ORR), which suffers from a minimum theoretical overpotential (-0.3 – 0.4 V) on a catalyst with a single type of active site due to the fixed but unsatisfactory adsorption-energy difference between OH* and OOH* intermediates^{26–28}. Over a model bimetallic Ag-supported Pd catalyst (Pd/Ag), both molecular dynamics studies and *in situ* characterizations reveal the interfacial spillover of adsorbed OH* from the Pd to another catalytic surface with weaker oxygen binding energy (that is, Ag) during the ORR, where proton–electron transfers of the OH* and OOH* intermediates separately occur on two different sites to completely circumvent their linear scaling relation. Furthermore, by replacing the Ag support with Ni(OH)₂, which owns a lower adsorption energy for OH*, Pd nanoparticles electrodeposited on Ni(OH)₂ (Pd/Ni(OH)₂) greatly boost the onset and half-wave potential of the ORR, to be not only superior to the theoretical limit of pure Pd, but also -70 mV higher than that of commercial Pt/C catalyst. Moreover, benefiting from the prompt removal of surface oxygenated species, Pd/Ni(OH)₂ prevents over-oxidation of the catalyst and shows excellent durability, with no activity decay after 30,000 potential cycles²⁹. In a similar way, the hybridized Fe/Co catalyst also overcomes the kinetic limitation of each component in the oxygen evolution reaction (OER), as evidenced by an extremely low Tafel slope of only 30.9 mV dec⁻¹.

Results

Theoretical prediction of OH*-spillover-based ORR pathway

The four-electron ORR to H₂O, an efficiency-limiting process in fuel cells and metal–air batteries, typically includes three oxygen-containing intermediates: OOH*, O* and OH* (ref. 30). Because all three intermediates are bound to the catalytic surface through an O atom, their adsorption free energies are correlated with each other in linear scaling relationships, and the adsorption-energy difference between OOH* and OH* is fixed at 3.2 ± 0.2 eV for most metals and oxides. Unfortunately, this is far from the optimal value of 2.46 eV, leading to an unavoidable non-zero overpotential^{31,32}. Based on ORR free-energy diagrams for the (111) surface of various metals in the periodic table adjacent to Pt, which is considered as the benchmark ORR electrocatalyst (Supplementary Fig. 1), a volcano-type activity plot can be constructed by using the Gibbs free energy for the adsorption of atomic oxygen (ΔG_{O^*}) as the descriptor, indicating a theoretically minimum thermodynamic overpotential of -0.3 V even at the crossing point (Fig. 1a).

For metals with strong ΔG_{O^*} , activities are limited by the reduction of OH*. On the other hand, for metals that bind oxygen weakly, the potential-determining step is the first associative adsorption of O₂ to form OOH*. As the adsorption energies of the three intermediates cannot vary independently on a single-component catalyst, an alternative reaction mechanism is proposed with synergistic multifunctional active sites that adsorb OOH* and OH* separately, and where a spillover effect can play a mediator role to transfer the intermediates (Supplementary Fig. 2). As illustrated schematically in Fig. 1b, there are three main steps in the spillover-based ORR pathway that can circumvent the scaling relationship between the adsorption energy of OOH* with OH* and optimize their respective values. The first step is the adsorption and activation of O₂ on the metal with a strong oxygen adsorption energy, followed by the diffusion and spillover of surface OH* to a secondary active site that accommodates it with weaker binding energy. The last step is reduction of the transferred OH* and desorption of the product on the secondary active site.

To experimentally determine the binding strength of the OH* adsorbate on different metal surfaces, cyclic voltammetry (CV) was conducted in an Ar-saturated electrolyte under the same electrochemical conditions, where the peak above -0.6 V (versus reversible hydrogen electrode (RHE)) corresponds to adsorption/desorption of the OH⁻ anion³³ (Supplementary Fig. 3). Deduced from the intensity of the OH⁻ adsorption peak, which is related to the coverage of OH*, the OH* binding strength follows the order Cu > Pd > Pt, consistent with results obtained using DFT calculations. In contrast, Ag and Au exhibit a weak binding energy for OH*, with a low surface reactivity with OH⁻, satisfying the prerequisite for the secondary active site. Compared to the most frequently adopted Pt, Pd is of particular interest as the primary ORR active site in this work not only considering its at least 50-fold earth abundance, but also because of its easier activation of O₂ and stronger adsorption of OH*, which can make Pd as an OH* reservoir for a higher surface coverage of intermediates to promote subsequent intermediate spillover^{34,35}. Nonetheless, noticeable barriers still need to be overcome regarding the diffusion of intermediates and spillover processes due to the resistance of the surface migration path and hybrid interface. Accordingly, the kinetic energy barriers were calculated to examine the possibility of O* or OH* diffusion on the Pd(111) surface between face-centred cubic (fcc), bridge and hexagonal close-packed (hcp) sites (Fig. 1c,d). It can be seen that a relatively high energy barrier of 0.57 eV is required to move O* from the fcc site to the bridge site of Pd(111). However, only a small driving force of 0.15 eV is required to achieve free diffusion of OH* on the Pd(111) surface, indicating the kinetic feasibility of OH* diffusion and suggesting that the generated O* intermediates from adsorbed OOH* during the ORR prefer to be reduced as OH* on the Pd sites, which subsequently accumulate and move on the Pd surface. Therefore, as long as there is another adjacent weak-adsorption catalytic surface that can abstract OH* from the interface, the OH*-spillover-based ORR pathway with cascaded O₂ activation and OH* desorption centres can be realized.

Spillover-mediated catalyst design

Given the weak OH* binding energy of Ag, an Ag-supported Pd catalyst (Pd/Ag) could be a promising candidate to achieve both thermodynamically and kinetically feasible OH* spillover and relayed desorption, hence promoting the overall ORR activity. Bimetallic Pd/Ag was directly grown on a conductive glassy carbon electrode (GDE) by simple electrodeposition at constant current, with Ag and Pd deposited in sequence to ensure a layer-by-layer structure. A transmission electron microscopy (TEM) image shows that the obtained Pd/Ag is composed of uniformly distributed small grains with dimensions of 4 – 6 nm (Supplementary Fig. 4). Well-resolved lattice fringes are observed in high-angle annular dark-field scanning transmission electron microscopy (HAADF-STEM) images of a representative nanoparticle (Fig. 2a), and these can be assigned to the interplanar spacing of the (111) plane of fcc Pd and

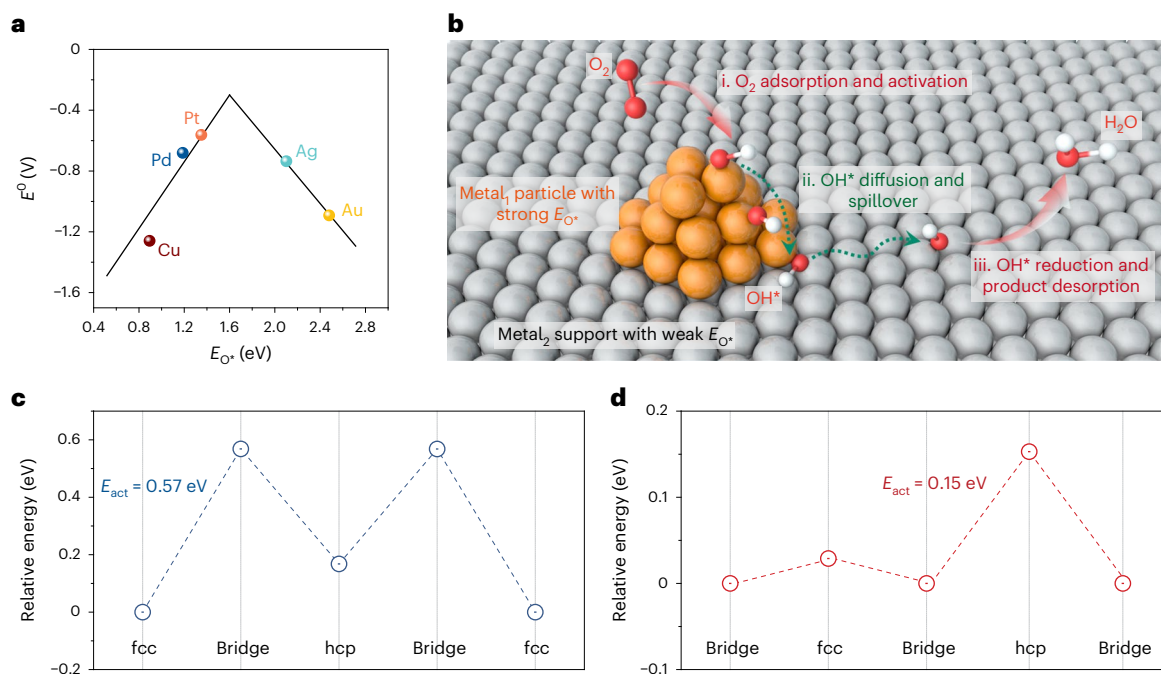


Fig. 1 | Theoretical design of the OH⁺-spillover-based ORR pathway. a, ORR activity volcano plot for metals adjacent to Pt in the periodic table of elements. **b**, Schematic illustration of the OH⁺-spillover-mediated ORR pathway. **c**, Potential energy profiles for O⁺ diffusion on the Pd(111) surface. **d**, Potential energy profiles for OH⁺ diffusion on the Pd(111) surface.

Ag. More importantly, this shows a clearly defined phase boundary between the Pd and Ag nanoparticles, revealing the presence of the binary-component interface³⁶. Synchrotron-based X-ray absorption near-edge structure (XANES) spectra were recorded at the Pd and Ag K-edges to further probe the valence state and local structure of the as-prepared Pd/Ag. As shown in Fig. 2b,c, the Pd and Ag K-edge XANES spectra for Pd/Ag are both nearly identical to that of the reference Pd and Ag foil, respectively, suggesting dominant metallic phases and no formation of a metal oxide/hydride in Pd/Ag. Fourier-transformed X-ray absorption fine structure (FT-EXAFS) spectra further show the absence of the characteristic peaks of Pd–Ag bonds in the bulk Pd/Ag (refs. 37,38) (Supplementary Fig. 5).

The ORR performance of Pd/Ag was subsequently evaluated in O₂-saturated 0.1 M KOH in a three-electrode electrochemical system. As shown in the linear sweep voltammetry (LSV) curves in Fig. 2d, electrodeposited pristine Pd and Ag exhibit poorer ORR activity than the benchmark Pt catalyst, consistent with their too strong (for Pd) and too weak (for Ag) binding to O⁺. On the other hand, Pd/Ag with the same metal loading not only elevates the ORR activity in comparison with both parent metals in terms of overpotential and limiting current density, but also outperforms the closest-to-optimum Pt with an ~50-mV lower half-wave potential (at ~2 mA cm⁻²), suggesting that the origin of this performance enhancement is far beyond the limit of the thermodynamic adsorption-energy modification of Pd or Ag alone. It is thus plausible that a novel pathway circumventing the linear scaling relations may be involved during the ORR on Pd/Ag. First, the same mass transport-limited current density of Pd/Ag as of Pt indicates their similar selectivity towards the four-electron transfer process³⁹. Binary-metallic catalysts consisting of Cu (which binds to O₂ more strongly than Pd) and Ag were also synthesized to demonstrate the important role of OH⁺ spillover in activity enhancement, with the size of the Cu nanoparticles being adjusted by means of the electrodeposition time. As shown in Supplementary Fig. 6a, the ORR activity of Cu/Ag is superior to that of pure Cu and Ag with the same amount of metal, as expected. However, on increasing the size of the Cu nanoparticles in Cu/Ag, both the ORR overpotential and limiting current density

become worse (Supplementary Fig. 6b), which can be ascribed to the migration of OH⁺ being the rate-determining step for the ORR on Cu/Ag owing to the extremely strong oxygen binding energy of Cu. When the diffusion distance is longer because of larger Cu nanoparticles, the inadequate OH⁺ supply will conversely limit ORR activity on the Cu/Ag.

Apart from the O₂ activation sites, the secondary catalytic component with weak oxygenated intermediate binding energy also plays a critical role in accelerating OH⁺ reduction to release OH⁻ in the ORR. Compared to metallic Ag, first-row (3d-block) nickel hydroxide (Ni(OH)₂) presents a lower adsorption energy for OH⁺ due to the more positive charge state of its four-coordinated Ni atoms, as revealed by its negligible surface reactivity to OH⁺ in CV and the free-energy diagram⁴⁰ (Supplementary Figs. 7–9). Ni(OH)₂-supported Pd (Pd/Ni(OH)₂) was thus constructed using the same electrodeposition method, and showed an additional improvement in intrinsic ORR activity (better than Pd/Ag; Supplementary Fig. 10 and Fig. 2e). To combine the advantages of large surface area and high electrical conductivity, Pd/Ni(OH)₂ was loaded on carbon black (Pd/Ni(OH)₂/C), achieving an ORR half-wave potential as high as 0.937 V (versus RHE), more positive than that of commercial Pt/C by ~70 mV. To provide a fair assessment of the intrinsic ORR activities on individual active sites, specific activities and mass activities were obtained by normalizing the kinetic currents at 0.9 V (versus RHE) to the electrochemically active surface area (ECSA) and mass loading of the active metal, respectively (Supplementary Figs. 11–13). As shown in Supplementary Fig. 14 and Supplementary Table 1, the specific activity and mass activity of Pd/Ni(OH)₂/C are enhanced by more than one order of magnitude over those of pure Pd and the benchmark Pt/C. More importantly, concomitant with the appearance of specific and mass activity improvements, there is also a striking decrease in the Tafel slope (from 64 mV dec⁻¹ for Pd to 48.8 mV dec⁻¹ for Pd/Ni(OH)₂/C) (Fig. 2f), suggesting faster ORR kinetics for Pd/Ni(OH)₂/C. Due to the multi-step nature of the ORR, it is difficult with Tafel analysis alone to pinpoint the exact kinetic features, so a homemade membrane electrode assembly (MEA)-based reactor was designed to carry out a time-resolved electrochemical study, in which both the transient current and response period could be recorded as

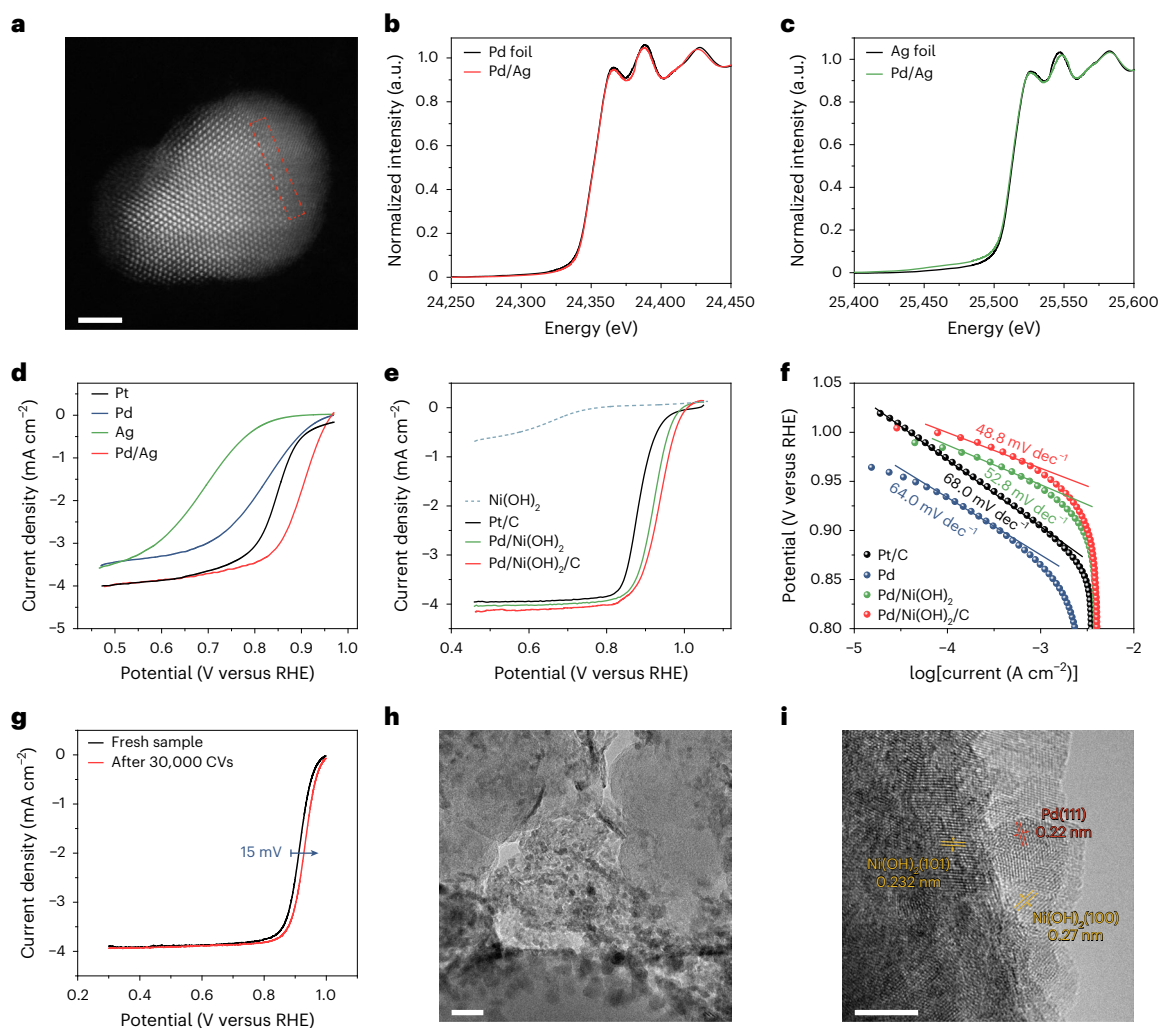


Fig. 2 | Structural characterization and ORR performance. **a**, Representative HAADF-STEM image showing a Pd/Ag particle. The interface between Pd and Ag is highlighted by the red dashed rectangle. Scale bar, 2 nm. **b**, XANES spectra of Pd/Ag and the reference Pd foil at the Pd K-edge. **c**, XANES spectra of Pd/Ag and the reference Ag foil at the Ag K-edge. **d**, ORR polarization curve of Pd/Ag in comparison with pure Pd, Ag and Pt. **e**, ORR polarization curves of Ni(OH)₂, Pd/Ni(OH)₂, Pd/Ni(OH)₂/C and commercial Pt/C. **f**, Corresponding Tafel plots

for Pd, Pd/Ni(OH)₂, Pd/Ni(OH)₂/C and commercial Pt/C. **g**, ORR polarization curves of Pd/Ni(OH)₂/C before and after 30,000 ADT cycles. All electrochemical data were acquired at a sweep rate of 5 mV s⁻¹ in O₂-saturated 0.1 M KOH with iR compensation. Rotation speed, 1,600 r.p.m. **h**, TEM image of Pd/Ni(OH)₂/C after the durability test. Scale bar, 20 nm. **i**, HRTEM image of Pd/Ni(OH)₂/C after the durability test. Scale bar, 5 nm.

kinetic fingerprints (Supplementary Fig. 15). When introducing the same dose of diluted O₂ to the cathode, Pd/Ni(OH)₂ had an obviously higher and sharper current in a shorter response period (~5.8 s) as compared to Pd, verifying the change in ORR reaction kinetics over the two catalytic systems.

Another key parameter for ORR performance is durability, and it is well known that the commercial Pt/C catalyst suffers greatly in this regard as a result of carbon corrosion and Pt dissolution, which can arise from attack by the OH* covering the Pt surface, because OH* desorption is the rate-determining step for Pt, consistent with the faster carbon oxidation rate of Pt/C at lower temperatures than that of pure carbon (C) in temperature-programmed oxidation (TPO) experiments^{29,41} (Supplementary Fig. 16). As a benchmark, the long-term stability of Pt/C was assessed by an accelerated durability test (ADT) under a continuous sweep rate of 100 mV s⁻¹ within the ORR potential window (between 0.45 and 1.05 V versus RHE) in O₂-saturated 0.1 M KOH. As shown in Supplementary Fig. 17a, the half-wave potential of the Pt/C is negatively shifted by 34 mV after 10,000 sweeping cycles. Moreover, the limiting current density becomes smaller due to carbon corrosion and Pt dissolution, as inferred from the loss in ECSA (Supplementary

Fig. 17b). Such phenomena can be visualized by comparing the morphology of Pt/C before and after the ADT (Supplementary Fig. 18). Pd/Ni(OH)₂/C demonstrates a substantial durability improvement, with almost identical limiting current density and an exciting positive shift of half-wave potential by 12 and 15 mV after 10,000 and even 30,000 sweeping cycles, respectively, due to surface activation (Supplementary Fig. 19 and Fig. 2g). As shown in the TEM images of Pd/Ni(OH)₂/C after the ADT (Fig. 2h,i), both C and Pd nanoparticles are well preserved, suggesting fast removal of oxidative OH* from the Pd surface in Pd/Ni(OH)₂/C during the ORR.

The results of microkinetic modelling suggest that the feasible OH* spillover from Pd to the Ag surface probably leads to the high ORR activity of Pd/Ag (Supplementary Fig. 20). To experimentally verify the intermediate spillover process during the ORR, it is necessary, but highly challenging, to trace the active oxygen species on the different catalytic surfaces during the reaction⁴². Inspired by the roughly proportional correlation between the orbital interaction extent of metal and oxygen with OH* coverage on the metal surface, in situ XANES can probe the local adsorption and diffusion of OH* on the bimetallic Pd/Ag model catalyst^{43,44}. Moreover, to more accurately monitor the

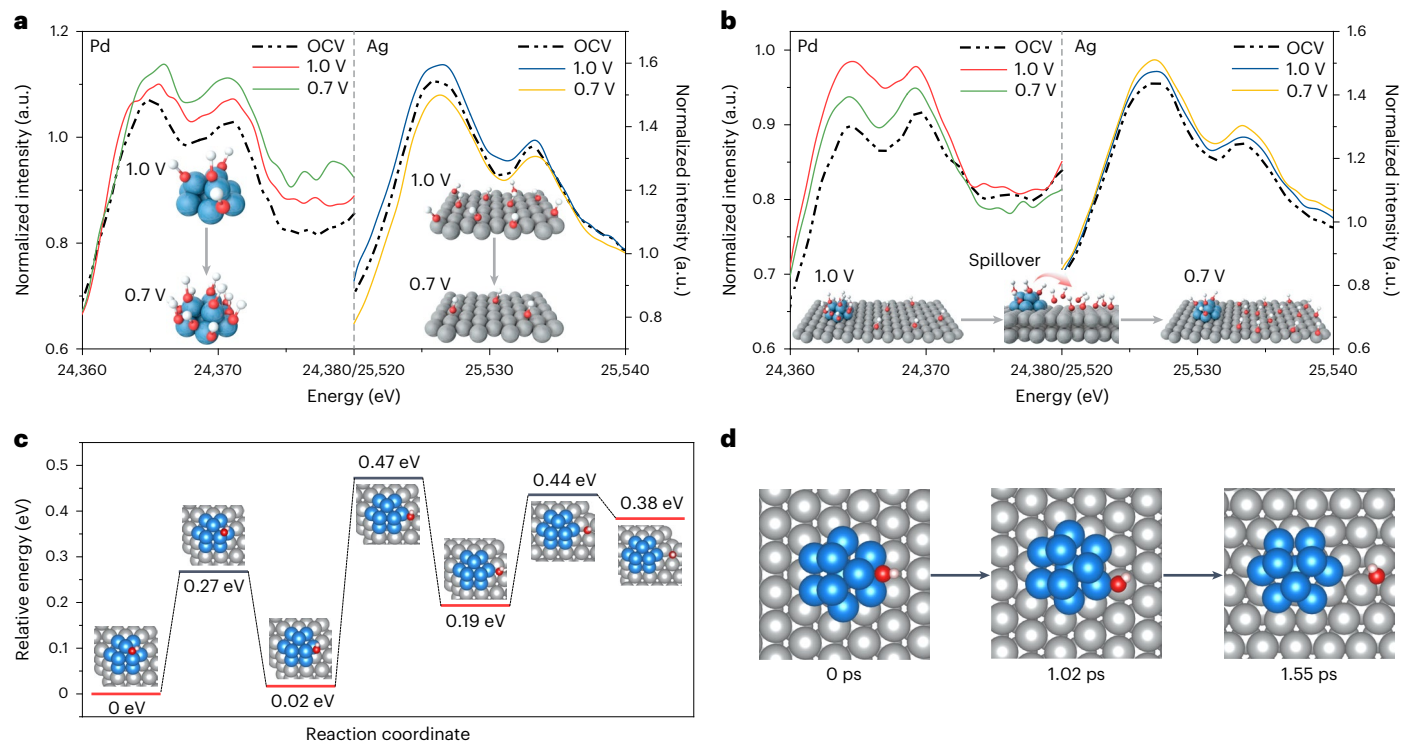


Fig. 3 | In situ HERFD X-ray absorption spectroscopy measurements and kinetic energy barrier calculations. a, Potential-dependent WL intensities of Pd K-edge HERFD-XANES for pristine Pd (left) and Ag K-edge HERFD-XANES for pristine Ag (right). **b**, Potential-dependent WL intensities of Pd K-edge HERFD-XANES for Pd/Ag (left) and Ag K-edge HERFD-XANES for Pd/Ag (right). All applied

potentials are referred to RHE. Insets in **a** and **b** present schematic illustrations of the correlation between OH* diffusion on Pd and Ag with in situ HERFD-XANES signals at different potentials. **c**, Energy profiles for OH* diffusion over a Pd₁₀ cluster, Pd/Ag interface and Ag(111) surface. **d**, Snapshots of OH* spillover from the Pd₁₀ cluster to the Ag(111) surface in AIMD.

subtle variations in XANES spectra upon adsorption of intermediates, high-energy-resolution fluorescence-detected XANES (HERFD-XANES) spectroscopy was applied, allowing a much better-resolved fine structure and more pronounced signature changes with different adsorption states⁴⁵ (Supplementary Fig. 21). Specially, the white-line (WL) intensity of the Pd or Ag K-edge spectrum can be attributed to Pd/Ag 5*p* and O 2*p* hybridization^{46,47} (Fig. 3a). For pristine Pd, the WL intensity is continuously enhanced from open-circuit voltage (OCV) to an applied potential of 1.0 V (versus RHE) and then to 0.7 V (versus RHE), suggesting steady accumulation of OH* on the Pd surface. By contrast, the WL intensity of weak-oxygen-adsorption Ag first increases from OCV to 1.0 V (versus RHE), but dramatically drops below the original value when the applied potential is further reduced to 0.7 V (versus RHE), indicating that although there is slight chemisorption of OOH* species before the reaction, the adsorption of intermediates is far slower than their consumption during the ORR, as supported by the aforementioned view that the rate-determining step of the ORR over Ag is the activation of O₂. To provide further evidence that OH* spillover takes place from OH*-enriched Pd to OH*-poor Ag sites across the Pd/Ag interface during the ORR, potential-dependent HERFD-XANES studies were performed at the K-edge of Pd and Ag on Pd/Ag (Fig. 3b). Compared to pristine Pd, the amplitude of WL for Pd in Pd/Ag at 0.7 V (versus RHE) becomes weaker than that at OCV after similar enhancement from OCV to 1.0 V (versus RHE), indicating faster removal of OH* than its generation on the Pd surface in Pd/Ag, which can possibly be ascribed to OH* migration to adjacent sites. At the same time, in contrast to the case with pristine Ag, a reverse trend in the increase in WL intensity is observed for Ag in Pd/Ag at 0.7 V (versus RHE). Given the OH* depletion on the pristine Ag surface during the ORR, such results unambiguously corroborate the spillover of OH* from Pd to Ag sites across their interfaces.

We also carried out DFT calculations to gain insights into the possibility of transferring the OH* adsorbed on Pd to the Ag surface

via a spillover process. A Pd₁₀ nanocluster supported on Ag(111) was thus constructed as a simplified model to resemble the experimental structure. The DFT results are summarized in Fig. 3c. It can be seen that only moderate energy barriers of 0.45 and 0.27 eV are required to drive free OH* diffusion on the surfaces of Pd and Ag, respectively, and these become even smaller if the OH* coverage is increased or the solvation environment is taken into account (Supplementary Figs. 22 and 23). Intriguingly, the spillover of OH* across the interface between Pd and Ag is shown to be a kinetically spontaneous process with almost zero barrier. Ab initio molecular dynamics (AIMD) simulations were conducted to examine the release of the adsorbed OH* on Pd sites to the nearby Ag surface (Fig. 3d, Supplementary Fig. 24 and Supplementary Video 1). In line with the in situ HERFD-XANES analysis, the AIMD simulation results unveil a rapid process of transferring adsorbed OH* from Pd to Ag sites; it takes only 1.02 ps to complete OH* spillover from one of the most stable adsorption sites on supported Pd to the Pd/Ag interface, then another 0.53 ps to diffuse onto the Ag surface, where the desorption of OH* occurs.

Extension of the intermediate-spillover-guided catalyst design

In the reverse process of the ORR, the linear adsorption-energy scaling relation between OOH* and OH* restricts the optimal single-component OER catalysts to precious Ir- and Ru-based oxides with a minimum theoretical overpotential of ~300–400 mV (refs. 3,48,49) (Fig. 4a). Although some impressive OER catalysts in alkaline electrolytes have been reported in recent years, such as oxyhydroxides, layered double hydroxides (LDHs) and perovskites, their non-uniform structural dimensions and flexible oxidation states make it difficult to refine the real active sites and accurate enhancement mechanisms^{50–52}. On further exploring first-row 3*d* transition metals as low-cost OER catalysts, it is interesting to find that the adsorption of OH* on Fe is the rate-determining step relative to the subsequent steps of the OER,

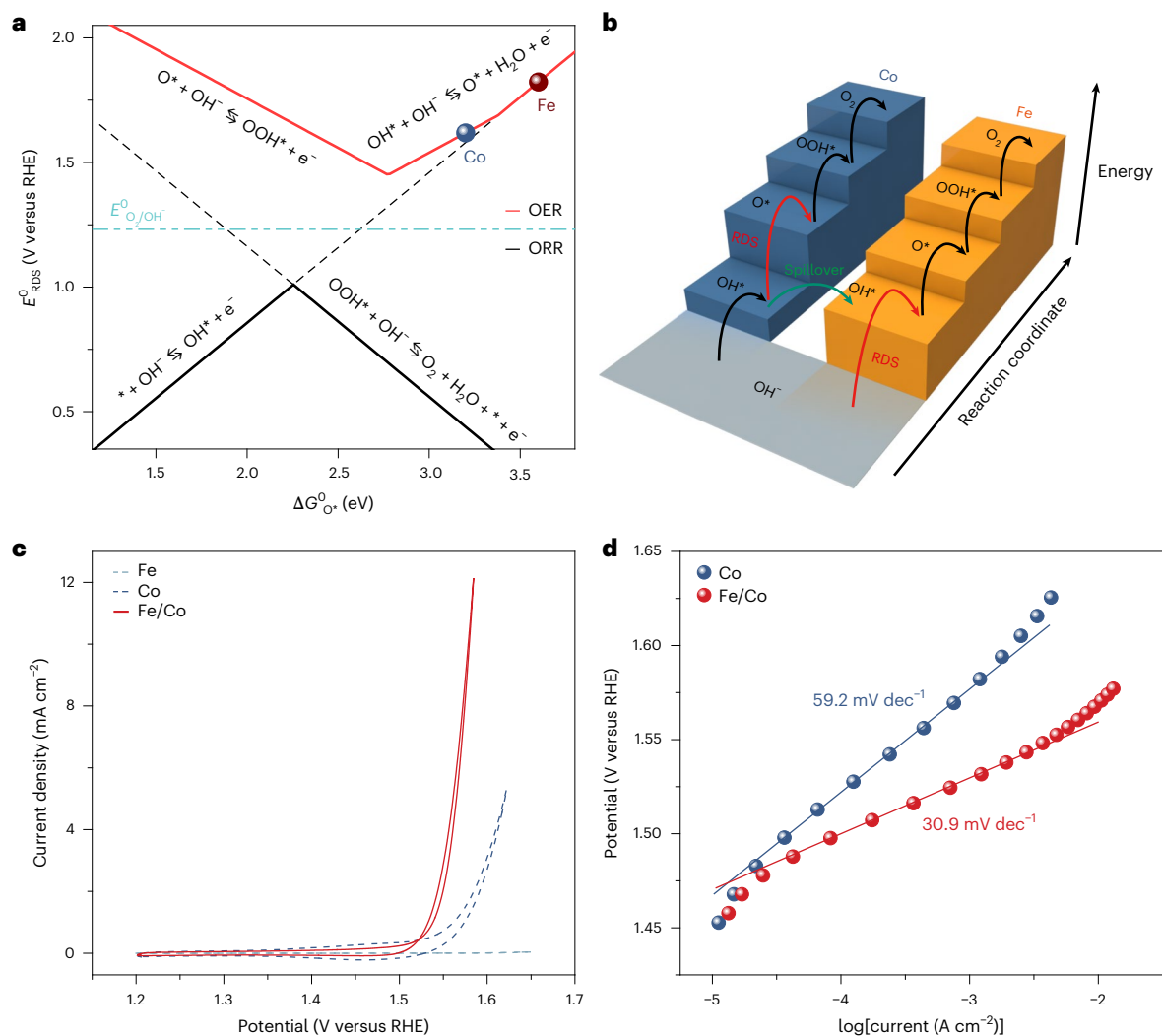


Fig. 4 | Intermediate-spillover-based OER pathway. **a**, Equilibrium potentials of elementary steps relative to the free binding energy of O^* ($\Delta G_{\text{O}^*}^0$) for the OER (top) and ORR (bottom). The corresponding positions of Fe and Co are indicated in the figure. **b**, OER free-energy diagrams of Fe and Co under an applied potential of $E = 0$ V (versus RHE). The designed OH^* -spillover-mediated OER pathway on

Fe/Co is highlighted by the green arrow. RDS, rate-determining step. **c**, Polarization curves of Fe/Co, pristine Fe and pristine Co acquired at a sweep rate of 5 mV s^{-1} in 1 M KOH . **d**, Tafel plots for Fe/Co and Co. All measurements were calibrated for i - R drop.

whereas for Co, the transformation of OH^* to O^* is the rate-determining step (Fig. 4b). In light of their distinctive rate-determining steps, Fe and Co are considered as potential candidates to be coupled via the proposed intermediate-spillover mechanism to relay and complete the overall reaction, where the accumulated OH^* on Co can be transferred onto Fe, and each component carries out its individual function in the OER. Using the same sequential electrodeposition method as before, Fe nanoparticles supported on Co catalysts (Fe/Co) were successfully prepared to fulfil the intermediate-spillover effect (Supplementary Fig. 25), with the Fe content optimized to balance the supply and consumption of OH^* . Compared to Fe/Co with 3.39 at% Fe, OER performance was inhibited no matter whether the content of Fe was decreased (1.68 at%) or increased (10.53 at%) owing to the excess and lack of transferred OH^* , respectively (Supplementary Fig. 26). As shown in Fig. 4c, Supplementary Figs. 27 and 28 and Supplementary Table 2, Fe/Co exhibits a superior OER activity than either pristine Fe or Co, as well as a very good turnover frequency (TOF) value compared to the benchmark transition-metal-based OER catalysts. It should be noted that Co and Fe can be easily oxidized to the oxyhydroxide phase during the OER (Supplementary Fig. 29), and DFT and AIMD simulations based on the FeOOH/CoOOH model verify the feasibility of attributing the intrinsic

activity enhancement to an OH^* -spillover-directed reaction pathway (Supplementary Figs. 30 and 31). More importantly, the exceptionally low Tafel slope of only 30.9 mV dec^{-1} for Fe/Co indicates that the OER rate-determining step of Fe/Co is switched to the pure chemical step between the electron-transfer steps of O^* and OOH^* formation, demonstrating that the proposed spillover-mediated OER pathway indeed occurs, circumventing the original rate-determining step of each individual component in Fe/Co (ref. 53) (Fig. 4d).

Discussion

In summary, we propose to decouple the elementary steps of multi-electron-transfer reactions on separate active centres through facile spillover of critical reaction intermediates, which helps circumvent the universal linear scaling relations between adsorption energies at an individual site. This catalyst design concept has been demonstrated on Pd/Ag, Pd/Ni(OH)₂ and Fe/Co catalysts for the ORR and OER, showing a substantial enhancement in activity and kinetics. Based on in situ HERFD-XANES and DFT calculations, OH^* is identified to be activated on a more oxophilic metal site, followed by its facile migration across the interface to an adjacent site with weaker oxygen binding energy, where the intermediate is relayed to complete the overall

catalytic cycle. Starting from these findings, the intermediate-spillover effect is anticipated to pave the way to break the linear-scaling limit of other multi-intermediate-involved heterogeneous chemical reactions.

Methods

Chemicals

Silver(I) nitrate ($\geq 99.0\%$, CAS no. 7761-88-8), palladium(II) chloride ($\geq 99.9\%$, CAS no. 7647-10-1), copper(II) sulfate ($\geq 99.99\%$ trace metals basis, CAS no. 7758-98-7), chloroplatinic acid hydrate ($\geq 99.9\%$ trace metals basis, CAS no. 26023-84-7), nickel(II) chloride (99.99% trace metals basis, CAS no. 7718-54-9), iron(III) chloride ($\geq 99.99\%$ trace metals basis, CAS no. 7705-08-0), cobalt(II) chloride (99.9% trace metals basis, CAS no. 7646-79-9), Pd (foil, 99.9% trace metals basis, CAS no. 7440-05-3), Ag (foil, 99.99% trace metals basis, CAS no. 7440-22-4) and potassium hydroxide (pellets, 99.99% trace metals basis, CAS no. 1310-58-3) were purchased from Sigma-Aldrich. Vulcan XC72 carbon black and Pt on Vulcan XC72 powder (20 wt%) were purchased from The Fuel Cell Store. All the chemicals were used without further purification. Deionized (DI) water ($15 \text{ M}\Omega \text{ cm}^{-1}$) passing through a Millipore Q water purification system was used in all experiments.

Catalyst preparation

The catalysts were prepared by galvanostatic electrodeposition using the chemical reagents AgNO_3 , PdCl_2 , CuSO_4 , $\text{H}_2\text{PtCl}_6 \cdot x\text{H}_2\text{O}$, NiCl_2 , FeCl_3 and CoCl_2 as precursors (the concentrations of all cations in electrolytes were 0.5 M). Monometallic catalyst-based samples were electrodeposited at a constant reduction current density of -1 mA cm^{-2} for 200 s, and binary-metallic catalysts were prepared by electrodeposition in series, with different reaction time ratios to adjust the contents of substrate and supported nanoparticles. Specifically, taking Pd/Ag as an example, the electrodeposition times of Pd and Ag were 20 and 200 s, respectively. The hydroxide-based catalysts were prepared with the aid of electrochemical reduction of solvents or oxygen, which caused a local pH increase for forming hydroxide precipitations. The current density for the hydroxide electrodeposition was kept at -5 mA cm^{-2} , and the reaction time was the same as that for metal-based catalysts.

Characterization

The morphological information was measured by TEM (JEOL JEM-2100F). XAFS measurements including XANES and EXAFS of the Pd K-edge and Ag K-edge were performed using a synchrotron radiation light source at the BL-12B2 beamline of SPring 8, NSRRC. Energy calibration was performed with a Pd or Ag foil standard by shifting all spectra to a glitch in the incident intensity.

In situ HERFD-XAFS measurements were conducted in a specially designed Teflon container with a window sealed by Kapton tape under identical conditions as the electrochemical measurements. For in situ experiments, the electrolyte (0.1 M KOH) in the cell was saturated with O_2 (99.99%), and a graphite rod and saturated calomel electrode (SCE) were used as the counter and reference electrodes, respectively. A carbon fibre paper electrode deposited with the catalyst was pressed in the electrolyte compartment of the cell. OCV, 1.0 V (versus RHE) and 0.7 V (versus RHE) were chosen as three representative conditions. The electrode was maintained under each condition for 30 min before recording the spectrum. The X-ray beam was transmitted through the tape, and the emitted fluorescence was selectively split by an analyser crystal. $K\alpha$ fluorescence signals from Pd and Ag were collected using a Si drift detector (XR-100CR Si-PIN X-ray detector) in partial fluorescence yield mode at BL-12XU of SPring 8, NSRRC.

Electrochemical measurements

All electrochemical measurements were carried out at ambient temperature and pressure on a CHI 760e potentiostat. A plastic cell was used to prevent contaminations such as Fe leaching of glass components. The 0.1 M KOH electrolyte solution was prepared from KOH pellets with

DI water. Specifically, for ORR tests, the electrolyte was saturated with O_2 (99.99%) by purging gas into aqueous solutions for 30 min, then maintaining the gas flow throughout the entire electrochemical measurements. The studied catalysts were prepared by electrodeposition as described above. A three-electrode cell configuration was employed with a working electrode comprising a glassy carbon rotating disk electrode (RDE, 5-mm diameter), a counter electrode of graphite rod, and a saturated calomel electrode (SCE) as the reference electrode. Before each experiment, the glassy carbon electrode was polished to a mirror shine with $0.05\text{-}\mu\text{m}$ alumina and cycled -50 times from -0.2 to 1.5 V (versus RHE) at a sweep rate of 300 mV s^{-1} in $0.5 \text{ M H}_2\text{SO}_4$. All potentials were referred to RHE for three-electrode testing unless otherwise noted. To ensure the accuracy of RHE, the reference electrode in H_2 -saturated 0.1 M KOH electrolyte was calibrated before conducting experiments. Additionally, for all the i - E curves reported in this study, the solution resistance R was measured via an iR compensation command, which was subsequently used to correct the solution ohmic loss by $E = E_{\text{measured}} - iR$. The reported current densities were normalized to the geometrical area of the electrode (mA cm^{-2}).

Before each ORR or OER test, several fast CV scans (200 mV s^{-1}) between 0.4 and 1.0 V (versus RHE, without i - R correction) were applied to remove the surface contaminants and thus to achieve an unperturbedly stable performance. In cases that were aimed to assess the activity from polarization curves, LSV measurements were performed at a rotation speed of $1,600 \text{ r.p.m.}$ and a low scan rate of 5 mV s^{-1} to obtain steady curves. All measurements were repeated three times to ensure reproducibility.

The ECSAs of the reported samples were determined by measuring the electrochemical double-layer capacitance (C_{dl}). Typically, CV scans were carried out at scan rates ranging from 10 to 200 mV s^{-1} in a non-Faradaic potential region. By plotting half of the net capacitive currents against the scan rates, the C_{dl} value was obtained as the corresponding slope, and the ECSA could be derived from

$$\text{ECSA} = S \times \frac{C_{\text{dl}}}{C_s} \quad (1)$$

where S is the surface area of the glassy carbon electrode (0.196 cm^2) and C_s is the specific capacitance for a flat surface. The C_s values for metal and hydroxide materials in alkaline conditions were in the range of $40\text{--}60 \mu\text{F cm}^{-2}$ when calculating the ECSA^{54,55}. To eliminate O_2 -diffusion limitations, the specific and mass activities of the studied ORR catalysts were quantified by normalizing kinetic currents at 0.9 V (versus RHE) to the corresponding ECSA and mass loading of the active metal (determined by inductively coupled plasma mass spectrometry). Mass transport-corrected kinetic currents were calculated using the Koutecký-Levich equation:

$$i_k = \frac{i_l \times i_{0.9}}{i_l - i_{0.9}} \quad (2)$$

where i_k is the kinetic current, i_l is the limiting current and $i_{0.9}$ is the measured current at a given potential of 0.9 V (versus RHE) after iR compensation^{56,57}. In our OER study, we used half amount of surface Fe and Co atoms as the active sites for the Fe/Co catalyst. The atom density of Fe and Co in the (111) facet of an fcc cell is

$$S_{\text{atom}} = \frac{2}{a^2} \quad (3)$$

where a is the dimension of the modelled facet. The molar number of atoms exposed on the Fe/Co surface was estimated from the ECSA and atom density by the following equation^{58,59}:

$$n = \frac{1}{2} \times \frac{\text{ECSA} \times S_{\text{atom}}}{N_A} \quad (4)$$

where N_A is Avogadro's constant ($6.02 \times 10^{23} \text{ mol}^{-1}$). The experimental TOF was then calculated from

$$\text{TOF} = \frac{i}{4 \times n \times F} \quad (5)$$

where i is the anodic current at a certain potential after iR compensation, the number 4 represents the four-electron transfer process of the OER, n is the molar number of active sites, and F is Faraday's constant ($96,485 \text{ C mol}^{-1}$)^{19,60}.

Computational details

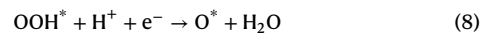
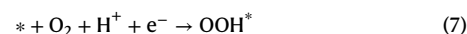
DFT calculations were carried out in the Vienna ab initio simulation package (VASP)^{61,62} using the projector augmented wave (PAW) pseudopotential for the core electrons⁶³, a 450-eV cutoff energy for the valence electrons, and the generalized gradient approximation (GGA) in the form of Perdew–Burke–Ernzerhof (PBE) for the exchange–correlation potentials^{49,50}. The convergence criteria for electronic and ionic iterations were set as 10^{-4} eV and $0.02 \text{ eV } \text{\AA}^{-1}$, respectively. The ORR process following a four-electron mechanism was studied on the (111) surfaces of Cu, Pd, Pt, Ag and Au, as well as a Pd particle supported on Ag(111). For each pure metal system, a (2×2) supercell was utilized, and for the model of a Pd particle supported on Ag, a Pd cluster consisting of ten atoms on a (5×5) Ag(111) surface was employed (referred to as $\text{Pd}_{10}@\text{Ag}(111)$). All slabs consisted of four atomic layers with $\sim 12 \text{ \AA}$ of vacuum layers. In the relaxation process, the upper two atomic layers and adsorbates were relaxed freely, while the bottom two layers were fixed at their bulk positions. k -meshes of $16 \times 16 \times 1$ and $3 \times 3 \times 1$ were chosen to sample the surface Brillouin zone for the upper and bottom layers, respectively. The gas-phase molecule was calculated in a box of $20 \times 20 \times 20 \text{ \AA}^3$ using only the Gamma point.

The transition states along different diffusion pathways were determined using the climbing image nudged elastic band method (CI-NEB)⁶⁴. To investigate the diffusion of OH^* species in $\text{Pd}_{10}@\text{Ag}(111)$ at low coverage, AIMD simulations were conducted in the canonical ensemble condition (NVT) ensemble at a temperature of 300 K, freely relaxing the Pd_{10} cluster. When studying the effect of OH^* coverage on its spillover from the supported Pd particle to the Ag(111) surface, the Pd_{10} cluster was fixed at its optimized configuration, as further relaxation would lead to fragmentation of the Pd_{10} cluster under high OH^* coverage. Due to the substantial computational demands required for running AIMD simulations on such a large system with more than 112 atoms, only the Gamma point of the Brillouin zone was sampled. The NVT was imposed through a Nosé–Hoover thermostat set with a target temperature of 300 K, and a time step of 1 fs was chosen^{65,66}. The AIMD simulation was performed for a total duration of 4 ps. The multiple-constrained molecular dynamics was implemented in VASP code. The cutoff energy of the plane-wave basis was set as 400 eV in the relaxation but 300 eV in simulations⁶⁷. The k -point grid of $3 \times 3 \times 1$ and Gamma ($1 \times 1 \times 1$)-centred k -mesh were sampled in relaxation and simulations, respectively. The free-energy profile along a collective variable (CV, ξ) was scanned using an approximate slow-growth approach with an explicit solvation model⁶⁸ (Supplementary Fig. 24a). The work required for the transformation from state 1 to state 2 could be integrated via the formula

$$W_{1 \rightarrow 2}^{\text{irrev}} = \int_{\xi_1}^{\xi_2} \left(\frac{\partial V(q)}{\partial \xi} \right) \cdot \xi d\xi \quad (6)$$

where ξ refers to the velocity of transformation and $\frac{\partial V(q)}{\partial \xi}$ is computed using the SHAKE algorithm⁶⁹. As ξ approaches an infinitesimally small value, $W_{1 \rightarrow 2}^{\text{irrev}}$ corresponds to the free-energy change between state 1 and state 2.

The associative mechanism for four-electron ORR comprises sequential addition of a proton and electron in each step:



The asterisk (*) denotes the active site on the catalyst. The free energy for each reaction intermediate is defined as

$$G = E_{\text{DFT}} + E_{\text{ZPE}} - \text{TS} \quad (11)$$

where E_{DFT} and E_{ZPE} represent the electronic energy calculated by DFT and zero-point energy estimated within the harmonic approximation, and TS denotes the entropy at 298.15 K ($T = 298.15 \text{ K}$). For the gas-phase molecule, the entropy was obtained directly from the standard thermodynamic database⁷⁰. However, for the chemisorbed species, the entropy correction was considered to be zero because the main contribution to entropy was from the translational component. The E_{DFT} , E_{ZPE} and TS of gas-phase molecules and reaction intermediates are listed in Supplementary Table 3.

For the reaction step containing the coupling of a proton and electron, the free energy of a proton and electron pair ($\text{H}^+ + \text{e}^-$) can be calculated as a function of applied potential relative to RHE (U versus RHE), that is, $\mu(\text{H}^+) + \mu(\text{e}^-) = 1/2\mu(\text{H}_2) - eU$, according to the computational hydrogen electrode (CHE) model⁷¹. Due to the well-known problem for DFT-GGA describing the triplet ground state of an O_2 molecule⁷², more accurate values for the H_2O and H_2 molecules as references, together with the experimental formation energy of H_2O (4.92 eV), were used to construct the free-energy diagram. The free energies of O_2 , OOH^* , O^* and OH^* at a given potential U relative to RHE were defined as

$$\Delta G(\text{O}_2) = 4.92 - 4eU \quad (12)$$

$$\Delta G(\text{OOH}) = G(\text{OOH}^*) + 3/2G(\text{H}_2) - G(*) - 2G(\text{H}_2\text{O}) - 3eU \quad (13)$$

$$\Delta G(\text{O}) = G(\text{O}^*) + G(\text{H}_2) - G(*) - G(\text{H}_2\text{O}) - 2eU \quad (14)$$

$$\Delta G(\text{OH}) = G(\text{OH}^*) + 1/2G(\text{H}_2) - G(*) - G(\text{H}_2\text{O}) - eU \quad (15)$$

In addition, the solvent effect, mainly derived from hydrogen-bonding between the H_2O molecules and reaction intermediates, has been reported to play an important role in the ORR. Accordingly, solvent correction values of 0.3, 0 and 0.5 eV were used for OOH^* , O^* and OH^* , respectively, in accordance with previous studies^{73,74}.

The atomic coordinates of the optimized computational models, and the initial and final configurations in the AIMD simulations, are provided in Supplementary Data 1.

Data availability

The data that support the findings of this study are available from the corresponding authors upon reasonable request. Source data are provided with this paper.

References

- Chu, S. & Majumdar, A. Opportunities and challenges for a sustainable energy future. *Nature* **488**, 294–303 (2012).
- Sabatier, P. *La Catalyse en Chimie Organique* (Librarie Polytechnique, 1913).

3. Seh, Z. W. et al. Combining theory and experiment in electrocatalysis: insights into materials design. *Science* **355**, eaad4998 (2017).
4. Nørskov, J. K., Bligaard, T., Rossmeisl, J. & Christensen, C. H. Towards the computational design of solid catalysts. *Nat. Chem.* **1**, 37–46 (2009).
5. Nørskov, J. K., Abild-Pedersen, F., Studt, F. & Bligaard, T. Density functional theory in surface chemistry and catalysis. *Proc. Natl Acad. Sci. USA* **108**, 937–943 (2011).
6. Bligaard, T. et al. The Brønsted–Evans–Polanyi relation and the volcano curve in heterogeneous catalysis. *J. Catal.* **224**, 206–217 (2004).
7. Abild-Pedersen, F. et al. Scaling properties of adsorption energies for hydrogen-containing molecules on transition-metal surfaces. *Phys. Rev. Lett.* **99**, 016105 (2007).
8. Zhao, Z.-J. et al. Theory-guided design of catalytic materials using scaling relationships and reactivity descriptors. *Nat. Rev. Mater.* **4**, 792–804 (2019).
9. Montoya, J. H. et al. Materials for solar fuels and chemicals. *Nat. Mater.* **16**, 70–81 (2017).
10. Wang, Q., Cheng, Y., Yang, H. B., Su, C. & Liu, B. Integrative catalytic pairs for efficient multi-intermediate catalysis. *Nat. Nanotechnol.* **19**, 1442–1451 (2024).
11. Wang, P. et al. Breaking scaling relations to achieve low-temperature ammonia synthesis through LiH-mediated nitrogen transfer and hydrogenation. *Nat. Chem.* **9**, 64–70 (2017).
12. Kibsgaard, J. & Chorkendorff, I. Considerations for the scaling-up of water splitting catalysts. *Nat. Energy* **4**, 430–433 (2019).
13. Wang, X. et al. Pivotal role of reversible NiO₆ geometric conversion in oxygen evolution. *Nature* **611**, 702–708 (2022).
14. Vojvodic, A. & Nørskov, J. K. New design paradigm for heterogeneous catalysts. *Natl Sci. Rev.* **2**, 140–143 (2015).
15. Khorshidi, A., Violet, J., Hashemi, J. & Peterson, A. A. How strain can break the scaling relations of catalysis. *Nat. Catal.* **1**, 263–268 (2018).
16. Pérez-Ramírez, J. & López, N. Strategies to break linear scaling relationships. *Nat. Catal.* **2**, 971–976 (2019).
17. Xiong, L. et al. Breaking the linear scaling relationship by compositional and structural crafting of ternary Cu–Au/Ag nanoframes for electrocatalytic ethylene production. *Angew. Chem. Int. Ed.* **60**, 2508–2518 (2021).
18. Gao, Q. et al. Breaking adsorption-energy scaling limitations of electrocatalytic nitrate reduction on intermetallic CuPd nanocubes by machine-learned insights. *Nat. Commun.* **13**, 2338 (2022).
19. Zhang, B. et al. Homogeneously dispersed multimetal oxygen-evolving catalysts. *Science* **352**, 333–337 (2016).
20. Wang, Q. et al. Atomic metal–non-metal catalytic pair drives efficient hydrogen oxidation catalysis in fuel cells. *Nat. Catal.* **6**, 916–926 (2023).
21. Xiong, M., Gao, Z. & Qin, Y. Spillover in heterogeneous catalysis: new insights and opportunities. *ACS Catal.* **11**, 3159–3172 (2021).
22. Jiang, L. et al. Facet engineering accelerates spillover hydrogenation on highly diluted metal nanocatalysts. *Nat. Nanotechnol.* **15**, 848–853 (2020).
23. Dai, J. et al. Hydrogen spillover in complex oxide multifunctional sites improves acidic hydrogen evolution electrocatalysis. *Nat. Commun.* **13**, 1189 (2022).
24. Shen, X. et al. Dual-site cascade oxygen reduction mechanism on SnO_x/Pt–Cu–Ni for promoting reaction kinetics. *J. Am. Chem. Soc.* **141**, 9463–9467 (2019).
25. Liu, Y. et al. Direct observation of accelerating hydrogen spillover via surface-lattice-confinement effect. *Nat. Commun.* **14**, 613 (2023).
26. Koper, M. T. M. Thermodynamic theory of multi-electron transfer reactions: implications for electrocatalysis. *J. Electroanal. Chem.* **660**, 254–260 (2011).
27. Yang, C.-L. et al. Sulfur-anchoring synthesis of platinum intermetallic nanoparticle catalysts for fuel cells. *Science* **374**, 459–464 (2021).
28. Gao, R. et al. Pt/Fe₂O₃ with Pt–Fe pair sites as a catalyst for oxygen reduction with ultralow Pt loading. *Nat. Energy* **6**, 614–623 (2021).
29. Lopes, P. P. et al. Eliminating dissolution of platinum-based electrocatalysts at the atomic scale. *Nat. Mater.* **19**, 1207–1214 (2020).
30. Debe, M. K. Electrocatalyst approaches and challenges for automotive fuel cells. *Nature* **486**, 43–51 (2012).
31. Christensen, R., Hansen, H. A., Dickens, C. F., Nørskov, J. K. & Vegge, T. Functional independent scaling relation for ORR/OER catalysts. *J. Phys. Chem. C* **120**, 24910–24916 (2016).
32. Zhang, J., Yang, H. B., Zhou, D. & Liu, B. Adsorption energy in oxygen electrocatalysis. *Chem. Rev.* **122**, 17028–17072 (2022).
33. Markovic, N., Gasteiger, H. & Ross, P. N. Kinetics of oxygen reduction on Pt(hkl) electrodes: implications for the crystallite size effect with supported Pt electrocatalysts. *J. Electrochem. Soc.* **144**, 1591 (1997).
34. Antolini, E. Palladium in fuel cell catalysis. *Energy Environ. Sci.* **2**, 915–931 (2009).
35. Yang, Y. et al. Combinatorial studies of palladium-based oxygen reduction electrocatalysts for alkaline fuel cells. *J. Am. Chem. Soc.* **142**, 3980–3988 (2020).
36. Zhang, J. et al. In situ precise tuning of bimetallic electronic effect for boosting oxygen reduction catalysis. *Nano Lett.* **21**, 7753–7760 (2021).
37. Mori, K. et al. Phenylamine-functionalized mesoporous silica supported PdAg nanoparticles: a dual heterogeneous catalyst for formic acid/CO₂-mediated chemical hydrogen delivery/storage. *Chem. Commun.* **53**, 4677–4680 (2017).
38. Mori, K., Sano, T., Kobayashi, H. & Yamashita, H. Surface engineering of a supported PdAg catalyst for hydrogenation of CO₂ to formic acid: elucidating the active Pd atoms in alloy nanoparticles. *J. Am. Chem. Soc.* **140**, 8902–8909 (2018).
39. Zamora Zeledón, J. A. et al. Tuning the electronic structure of Ag–Pd alloys to enhance performance for alkaline oxygen reduction. *Nat. Commun.* **12**, 620 (2021).
40. Wang, X. P. et al. Strain stabilized nickel hydroxide nanoribbons for efficient water splitting. *Energy Environ. Sci.* **13**, 229–237 (2020).
41. Wang, Q. et al. Long-term stability challenges and opportunities in acidic oxygen evolution electrocatalysis. *Angew. Chem. Int. Ed.* **62**, e202216645 (2023).
42. Dong, J.-C. et al. In situ Raman spectroscopic evidence for oxygen reduction reaction intermediates at platinum single-crystal surfaces. *Nat. Energy* **4**, 60–67 (2019).
43. Zhang, X.-L. et al. Strongly coupled cobalt diselenide monolayers for selective electrocatalytic oxygen reduction to H₂O₂ under acidic conditions. *Angew. Chem. Int. Ed.* **60**, 26922–26931 (2021).
44. Yang, J. et al. Dynamic behavior of single-atom catalysts in electrocatalysis: identification of Cu–N₃ as an active site for the oxygen reduction reaction. *J. Am. Chem. Soc.* **143**, 14530–14539 (2021).
45. Tromp, M. et al. High energy resolution fluorescence detection X-ray absorption spectroscopy: detection of adsorption sites in supported metal catalysts. *AIP Conf. Proc.* **882**, 651–653 (2007).

46. Wang, J., Zhou, J., Hu, Y. & Regier, T. Chemical interaction and imaging of single Co_3O_4 /graphene sheets studied by scanning transmission X-ray microscopy and X-ray absorption spectroscopy. *Energy Environ. Sci.* **6**, 926–934 (2013).
47. Gaur, A. & Shrivastava, B. D. Speciation using X-ray absorption fine structure (XAFS). *Rev. J. Chem.* **5**, 361–398 (2015).
48. Wang, Q. et al. Coordination engineering of iridium nanocluster bifunctional electrocatalyst for highly efficient and pH-universal overall water splitting. *Nat. Commun.* **11**, 4246 (2020).
49. Wang, J. et al. Exceptionally active and stable RuO_2 with interstitial carbon for water oxidation in acid. *Chem* **8**, 1673–1687 (2022).
50. Wu, T. et al. Iron-facilitated dynamic active-site generation on spinel CoAl_2O_4 with self-termination of surface reconstruction for water oxidation. *Nat. Catal.* **2**, 763–772 (2019).
51. Peng, L. et al. Atomic cation-vacancy engineering of NiFe-layered double hydroxides for improved activity and stability towards the oxygen evolution reaction. *Angew. Chem. Int. Ed.* **60**, 24612–24619 (2021).
52. Zhu, Y. et al. Oxygen activation on Ba-containing perovskite materials. *Sci. Adv.* **8**, eabn4072 (2022).
53. Zhang, J. et al. Advances in thermodynamic-kinetic model for analyzing the oxygen evolution reaction. *ACS Catal.* **10**, 8597–8610 (2020).
54. Wang, J. et al. Redirecting dynamic surface restructuring of a layered transition metal oxide catalyst for superior water oxidation. *Nat. Catal.* **4**, 212–222 (2021).
55. Jin, Z. et al. Understanding the inter-site distance effect in single-atom catalysts for oxygen electroreduction. *Nat. Catal.* **4**, 615–622 (2021).
56. Luo, M. et al. PdMo bimetallic for oxygen reduction catalysis. *Nature* **574**, 81–85 (2019).
57. Liang, J. et al. Gas-balancing adsorption strategy towards noble-metal-based nanowire electrocatalysts. *Nat. Catal.* **7**, 719–732 (2024).
58. Liu, C. et al. Oxygen evolution reaction over catalytic single-site Co in a well-defined brookite TiO_2 nanorod surface. *Nat. Catal.* **4**, 36–45 (2021).
59. Liu, S. et al. A top-down strategy for amorphization of hydroxyl compounds for electrocatalytic oxygen evolution. *Nat. Commun.* **13**, 1187 (2022).
60. Zhang, B. et al. High-valence metals improve oxygen evolution reaction performance by modulating 3d metal oxidation cycle energetics. *Nat. Catal.* **3**, 985–992 (2020).
61. Kresse, G. & Furthmüller, J. Efficient iterative schemes for ab initio total-energy calculations using a plane-wave basis set. *Phys. Rev. B* **54**, 11169–11186 (1996).
62. Kresse, G. & Furthmüller, J. Efficiency of ab-initio total energy calculations for metals and semiconductors using a plane-wave basis set. *Comput. Mater. Sci.* **6**, 15–50 (1996).
63. Kresse, G. & Joubert, D. From ultrasoft pseudopotentials to the projector augmented-wave method. *Phys. Rev. B* **59**, 1758–1775 (1999).
64. Henkelman, G., Uberuaga, B. P. & Jónsson, H. A climbing image nudged elastic band method for finding saddle points and minimum energy paths. *J. Chem. Phys.* **113**, 9901–9904 (2000).
65. Nosé, S. A unified formulation of the constant temperature molecular dynamics methods. *J. Chem. Phys.* **81**, 511–519 (1984).
66. Hoover, W. G. Canonical dynamics: equilibrium phase-space distributions. *Phys. Rev. A* **31**, 1695–1697 (1985).
67. VandeVondele, J. & Hutter, J. Gaussian basis sets for accurate calculations on molecular systems in gas and condensed phases. *J. Chem. Phys.* **127**, 114105 (2007).
68. Woo, T. K., Margl, P. M., Blöchl, P. E. & Ziegler, T. A combined Car-Parrinello QM/MM implementation for ab initio molecular dynamics simulations of extended systems: application to transition metal catalysis. *J. Phys. Chem. B* **101**, 7877–7880 (1997).
69. Sprik, M. & Ciccotti, G. Free energy from constrained molecular dynamics. *J. Chem. Phys.* **109**, 7737–7744 (1998).
70. Cramer, C. J. *Essentials of Computational Chemistry: Theories and Models* 2nd edn (Wiley, 2004).
71. Nørskov, J. K. et al. Origin of the overpotential for oxygen reduction at a fuel-cell cathode. *J. Phys. Chem. B* **108**, 17886–17892 (2004).
72. Jones, R. O. & Gunnarsson, O. The density functional formalism, its applications and prospects. *Rev. Mod. Phys.* **61**, 689–746 (1989).
73. Greeley, J. et al. Alloys of platinum and early transition metals as oxygen reduction electrocatalysts. *Nat. Chem.* **1**, 552–556 (2009).
74. Viswanathan, V., Hansen, H. A., Rossmeisl, J. & Nørskov, J. K. Universality in oxygen reduction electrocatalysis on metal surfaces. *ACS Catal.* **2**, 1654–1660 (2012).

Acknowledgements

This work was supported financially by the City University of Hong Kong startup fund (9020003), an ITF-RTH–Global STEM Professorship (9446006), and the JC STEM lab of Advanced CO_2 Upcycling (9228005). S.-F.H. acknowledges financial support from the National Science and Technology Council, Taiwan (contract no. NSTC 111-2628-M-A49-008) and Yushan Young Scholar Program and the Center for Emergent Functional Matter Science, Ministry of Education, Taiwan. H.B.T. acknowledges financial support from the National Key R&D Program of China (2023YFB4004600). H.B.Y. acknowledges support from the National Natural Science Foundation of China under grant no. 22075195. W.L. is grateful for support from the National Natural Science Foundation of China (22427801). Y.X. acknowledges financial support from the National Natural Science Foundation of China (22478348). C.S. is financially supported by the National Key Research and Development Program of China (2021YFA1600800). J.G.C. is sponsored by the US Department of Energy (contract no. DE-SC0012704).

Author contributions

Q.W., H.B.T. and B.L. conceived and designed the project. Q.W., K.L., H.B.T., L.Z., J.Z., Y.C., J.C. and Y.X. performed the catalyst synthesis, structural characterizations and electrochemical measurements. S.-F.H., H.B.Y., N.H. and Y.L. acquired the X-ray absorption spectroscopies and provided expertise for data analysis. W.L. and W.W. obtained the TEM images. X.H. and F.L. carried out the theoretical calculations. Q.W., H.B.T., C.S., J.G.C. and B.L. discussed the results and drafted the paper. All authors reviewed and contributed to this paper.

Competing interests

The authors declare no competing interests.

Additional information

Supplementary information The online version contains supplementary material available at <https://doi.org/10.1038/s41929-025-01323-8>.

Correspondence and requests for materials should be addressed to Hua Bing Tao, Jingguang G. Chen or Bin Liu.

Peer review information *Nature Catalysis* thanks the anonymous reviewers for their contribution to the peer review of this work.

Reprints and permissions information is available at www.nature.com/reprints.

Publisher's note Springer Nature remains neutral with regard to jurisdictional claims in published maps and institutional affiliations.

Springer Nature or its licensor (e.g. a society or other partner) holds exclusive rights to this article under a publishing agreement with

the author(s) or other rightsholder(s); author self-archiving of the accepted manuscript version of this article is solely governed by the terms of such publishing agreement and applicable law.

© The Author(s), under exclusive licence to Springer Nature Limited 2025

¹Department of Materials Science and Engineering, City University of Hong Kong, Hong Kong SAR, China. ²Department of Applied Chemistry and Center for Emergent Functional Matter Science, National Yang Ming Chiao Tung University, Hsinchu, Taiwan. ³Department of Medicinal and Applied Chemistry, Kaohsiung Medical University, Kaohsiung, Taiwan. ⁴State Key Laboratory for Physical Chemistry of Solid Surfaces, Collaborative Innovation Center of Chemistry for Energy Materials, and College of Chemistry and Chemical Engineering, Xiamen University, Xiamen, China. ⁵Innovation Laboratory for Sciences and Technologies of Energy Materials of Fujian Province (IKKEM), Xiamen, China. ⁶School of Chemistry, Chemical Engineering and Biotechnology, Nanyang Technological University, Singapore, Singapore. ⁷School of Materials Science and Engineering, Suzhou University of Science and Technology, Suzhou, China. ⁸Dalian Institute of Chemical Physics, Chinese Academy of Sciences, Dalian, China. ⁹School of Chemical Engineering, Dalian University of Technology, Dalian, China. ¹⁰National Synchrotron Radiation Research Center, Hsinchu, Taiwan. ¹¹Institute of Coal Chemistry, Chinese Academy of Sciences, Taiyuan, China. ¹²College of Chemical Engineering, Zhejiang University of Technology, Hangzhou, China. ¹³International Collaboration Laboratory of 2D Materials for Optoelectronics Science and Technology of Ministry of Education, Institute of Microscale Optoelectronics, Shenzhen University, Shenzhen, China. ¹⁴Department of Chemical Engineering, Columbia University, New York, NY, USA. ¹⁵Department of Chemistry, Hong Kong Institute for Clean Energy (HKICE) & Center of Super-Diamond and Advanced Films (COSDAF), City University of Hong Kong, Hong Kong SAR, China. ¹⁶These authors contributed equally: Qilun Wang, Sung-Fu Hung, Kejie Lao. ✉e-mail: hbtiao@xmu.edu.cn; jgchen@columbia.edu; blui48@cityu.edu.hk